Action-angle formulation of generalized, orbit-based, fast-ion diagnostic weight functions

L. Stagner and W. W. Heidbrink
University of California Irvine, Irvine, California 92867, USA

(Received 14 June 2017; accepted 2 August 2017; published online 14 August 2017)

Due to the usually complicated and anisotropic nature of the fast-ion distribution function, diagnostic velocity-space weight functions, which indicate the sensitivity of a diagnostic to different fast-ion velocities, are used to facilitate the analysis of experimental data. Additionally, when velocity-space weight functions are discretized, a linear equation relating the fast-ion density and the expected diagnostic signal is formed. In a technique known as velocity-space tomography, many measurements can be combined to create an ill-conditioned system of linear equations that can be solved using various computational methods. However, when velocity-space weight functions (which by definition ignore spatial dependencies) are used, velocity-space tomography is restricted, both by the accuracy of its forward model and also by the availability of spatially overlapping diagnostic measurements. In this work, we extend velocity-space weight functions to a full 6D generalized coordinate system and then show how to reduce them to a 3D orbit-space without loss of generality using an action-angle formulation. Furthermore, we show how diagnostic orbit-weight functions can be used to infer the full fast-ion distribution function, i.e., orbit tomography. In depth derivations of orbit weight functions for the neutron, neutral particle analyzer, and fast-ion D-α diagnostics are also shown. *Published by AIP Publishing*. [http://dx.doi.org/10.1063/1.4990391]

I. BACKGROUND AND MOTIVATION

From a diagnostics standpoint, fast-ion physics is particularly difficult. Unlike bulk-ion diagnostics that measure Maxwellian distributed velocities, fast-ion diagnostics have to measure a velocity distribution that can be highly anisotropic due to the neutral beam and RF heating. The lack of a simple parametrization of the fast-ion velocity distribution makes it difficult to draw correlations between experimental data and the relevant fast-ion physics. In an effort to aid the modeling, interpretation, and experimental design of fast-ion diagnostics, the following *ansatz* was proposed:[1]

$$S = \int\int W(E,p)F(E,p)\,dEdp, \tag{1}$$

where S is the diagnostic signal, $F(E,\ p)$ is the fast-ion energy-pitch distribution function, and $W(E,\ p)$ is a diagnostic weighting function. The weight function indicates the phase-space sensitivity of the diagnostic, allowing for easier interpretation of the diagnostic data (Fig. 1). Since their introduction there has been a focused effort in calculating velocity-space weight functions for more fast-ion diagnostics.[2–6] Additionally, in a process called velocity-space tomography,[2,7–9] the velocity-space fast-ion distribution function can be inferred by discretizing Eq. (1), creating a system of linear equations that can be solved using various computational methods.[10] This powerful method has been used to study the redistribution of fast ions during sawtooth crashes.[10–12]

In this paper, the concept of velocity-space weight functions is extended to encompass the entire phase space. The motivation for this extension is threefold. First, most velocity-space weight functions assume a fixed spatial location or average over the measurement volume of the diagnostic. In regions where the fast-ion distribution has large spatial variations, Eq. (1) performs poorly (Sec. III D). A generalization of Eq. (1) to include spatial coordinates is needed to properly model diagnostics in these regions. Second, fast-ion orbits link velocity and configuration space. When an orbit traverses two different measurement volumes, a measurement at one location contains information about the velocity distribution at the other. As shown in a forthcoming publication, inclusion of this additional information improves the accuracy of the distribution-function inversions. Third, velocity-space tomography requires overlapping diagnostic views. In practice, due to limited port access, radial arrays from one or two ports are often easier to implement than multiple views of the same spatial volume from different viewing locations. Orbit weight functions enable velocity-space inference from radial detector arrays.

Section II presents the theoretical framework for orbit weight functions. In Sec. II A, a generalized 6-dimensional diagnostic weight function is derived. In Sec. II B, the dimensionality of the 6D weight function is reduced to a 3D orbit weight function without loss of generality through an action-angle formulation of the guiding center motion of a fast ion. Section III presents a representative application. Section III A describes the DIII-D diagnostics and plasma for the selected case. Then, in Secs. III B–III D, orbit weight functions are illustrated for neutron, neutral-particle analyzer, and fast-ion D-α (FIDA) diagnostics. Conclusions appear in Sec. IV. The collisional-radiative model used to describe the neutral particle analyzer (NPA) and FIDA diagnostics is summarized in the Appendix.

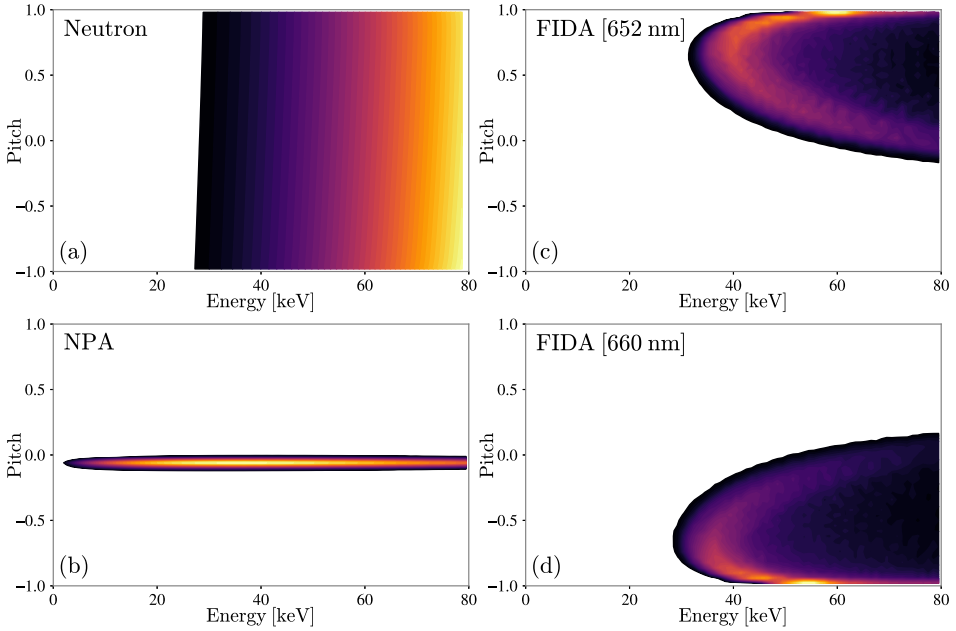

FIG. 1. Representative velocity-space weight functions for the DIII-D plasma and diagnostics described in Sec. III A. (a) The neutron scintillator is a global measurement of the neutron production rate. Its weight function is spatially averaged and shows a strong energy dependence. The slight anisotropy in pitch is due to fast ions traveling with (positive pitch) and against (negative pitch) the plasma rotation. (b) The neutral particle analyzer (NPA) diagnostic detects neutralized fast ions that escape the plasma. The collimation of the detector only permits a small range of pitch values to hit the detector and, because the detector is operated in current mode, the weight function is sensitive to many different energies. (c) and (d) The fast-ion deuterium-α (FIDA) diagnostic measures spectra produced by neutralized fast ions. The weight function depends upon wavelength. These FIDA weight functions are line-of-sight averaged at $\lambda = (652, 660) \pm 0.2$ nm for a single oblique (Fig. 4) viewing chord.

II. THEORETICAL FRAMEWORK

A. Generalized diagnostic weight functions

Consider a fast ion with phase-space coordinates $\mathbf{x} = [\mathbf{p}, \mathbf{q}]$, where $\mathbf{p}$ and $\mathbf{q}$ are the generalized momentum and position, respectively. For any given fast-ion diagnostic, there is a function, $S(\mathbf{x})$, that gives the expected signal produced by each fast ion. The expected total diagnostic signal is given by summing the contributions of all fast ions

$$S_{tot} = \sum_{k=1}^{N} S(\mathbf{x}_k), \tag{2}$$

where N is the total number of fast ions. This equation can be expressed in terms of the frequency in which $\mathbf{x}$ occurs

$$S_{tot} = N \sum_{\mathbf{x}_k \in R_X} S(\mathbf{x}_k) P_X(\mathbf{x}_k), \tag{3}$$

where $P_X(\mathbf{x}_k)$ is the frequency of $\mathbf{x}_k$ occurring. In the continuum limit, the discrete sum in the above equation can be replaced by an integral and can be written in the form

$$S_{tot} = \int S(\mathbf{x}) N \sum_{\mathbf{x}_k \in R_X} P_X(\mathbf{x}_k) \delta(\mathbf{x} - \mathbf{x}_k) d\mathbf{x} = \int S(\mathbf{x}) F(\mathbf{x}) d\mathbf{x}, \tag{4}$$

where $F(\mathbf{x})$ is the fast-ion distribution function. By inspection, it is clear that Eq. (4) is the generalized version of Eq. (1) and that weight functions are just the expected diagnostic signal for a given phase-space coordinate.

If we consider the phase-space coordinate system $\mathbf{x} = \{E, p, \gamma, R, z, \phi\}$, where E is the energy, p is the pitch with respect to the plasma current ($p = v_\parallel / v$), γ is the gyro-angle, R is the major radius, z is the elevation, and ϕ is the toroidal angle, the velocity-space weight function in Eq. (1) can be recovered by averaging over the unused phase-space variables. Since most velocity-space weight functions are gyro-averaged and spatially localized, the following reduction of Eq. (4) reproduces the velocity-space weight function:

$$W(E,p) = \frac{1}{2\pi} \int\int\int\int S(E,p,\gamma,R,z,\phi) \delta(R - R_0) \delta(z - z_0) \times \delta(\phi - \phi_0)\, d\gamma\, dR\, dz\, d\phi. \tag{5}$$

In this framework, $W(E, p)$ is interpreted to be the average signal produced by a fast ion with a given energy and pitch.

B. Orbit weight functions

A reduction of the phase-space, as done in Eq. (5), greatly simplifies analysis and facilitates tomographic reconstructions by reducing the number of unknown parameters. However, since we are concerned about the motion of the fast ions, care must be taken to ensure that no critical information is lost when averaging over variables. In other words, only variables that do not appear in the Lagrangian (i.e., ignorable or cyclic coordinates) can be averaged out without critical information loss. By this standard, the phase-space reduction done in Eq. (5) is inadequate since only the gyro and toroidal angle averaging were permissible.

In order to reduce the phase-space as much as possible it is advantageous to express the expected diagnostic signal, S, in canonical action-angle coordinates, $\mathbf{x} = (\mathbf{J}, \boldsymbol{\Theta})$. Action-angle coordinates are a set of canonical coordinates with the special

property that the action variables, $\mathbf{J}$, are invariants of the motion and the angle coordinates, $\boldsymbol{\Theta}$, are cyclic/ignorable and can be averaged over. In these coordinates, information preserving phase-space reductions can then be succinctly expressed as

$$W(\mathbf{J}) = \left(\prod_i \frac{1}{\tau_i}\right) \int_0^{\tau_1} \dots \int_0^{\tau_i} S(\mathbf{J}, \boldsymbol{\Theta})\, d\boldsymbol{\Theta}, \tag{6}$$

where τ_i are the periods of the angle coordinates. In this framework, $W(\mathbf{J})$ is interpreted as the average signal produced by a fast ion with action coordinates $\mathbf{J}$.

The total diagnostic signal can be calculated using these reduced weight functions. Consider the subset of fast ions in a plasma with action coordinates, $\mathbf{J}_k$. The signal produced by these fast ions is given by

$$S_k = \sum_i^{N_k} S(\mathbf{J}_k, \boldsymbol{\Theta}_i) = N_k \sum_i^{N_k} S(\mathbf{J}_k, \boldsymbol{\Theta}_i)/N_k, \tag{7}$$

where N_k is the number of fast ions with action coordinates $\mathbf{J}_k$. The sum on the right-hand side is the average signal produced by the subset of fast ions. This is identical to the interpretation of the reduced weight function. The total diagnostic signal can then be expressed as

$$S_{tot} = \sum_k N_k W(\mathbf{J}_k). \tag{8}$$

In the context of guiding center motion, $\mathbf{J}_k$ acts as a label for an individual fast-ion orbit. Therefore, Eq. (8) can be interpreted as a sum of the signal produced by each fast-ion orbit. As in velocity-space tomography, when there are multiple measurements, Eq. (8) can be put into matrix form, creating a system of linear equations that can be solved. We call this orbit tomography.

An action-angle parametrization of the guiding center motion of a fast ion in a tokamak has three action coordinates and three angle coordinates. There are many possible choices for action-angle coordinates; the classical choice being the canonical constants of motion: energy, magnetic moment, and toroidal canonical angular momentum, $\mathbf{J} = (E,\ \mu,\ p_\phi)$. However, due to an ambiguity in the sign of $v_\parallel$ in the definition of p_ϕ, the classical choice of coordinates does not always *uniquely* label distinct orbits, i.e., a single action coordinate $\mathbf{J}_k$ in this space could correspond to two different orbit trajectories. This makes it difficult to use Eq. (6) to reduce the phase-space since the angle variables would have different periods. Instead, we use a modified version of the coordinates first promoted by Rome[13] and others.[14] Here, we define the action coordinates, hereby called orbit-space variables, to be

$$\mathbf{J} = (E, p_m, R_m), \tag{9}$$

where E is the energy, R_m is the maximal radius along the orbit, and p_m is the pitch with respect to the plasma current at R_m. The suitable angle variables, which describe the position of the fast ion along the orbit, are

$$\boldsymbol{\Theta} = (t, \gamma, \phi_0), \tag{10}$$

where t is the time, γ is the gyro-phase, and ϕ_0 is the initial toroidal angle. Applying Eq. (6) yields the general definition of an orbit weight function

$$W(E, p_m, R_m) = \frac{1}{4\pi^2 \tau_p} \int_0^{2\pi} \int_0^{2\pi} \int_0^{\tau_p} S(E, p_m, R_m, t, \gamma, \phi_0)\, dt\, d\gamma\, d\phi_0, \tag{11}$$

where τ_p is the poloidal transit time.

This choice of orbit-space coordinates has several nice properties. The space has natural boundaries in all three coordinates ($E = [0,\ E_{max}]$, $R_m = [R_{axis},\ R_{wall}]$, and $p_m = [-1,\ 1]$), which makes it easy to enumerate all possible orbit trajectories for a given magnetic equilibrium. Additionally, as can be seen in the topological map of the orbit-space in Fig. 2, counter-passing orbits are easily identified by the sign of p_m.

III. ORBIT WEIGHT FUNCTIONS FOR VARIOUS FAST-ION DIAGNOSTICS

In this section, after briefly describing the plasma conditions and diagnostics, orbit weight functions are derived for three DIII-D fast-ion diagnostics: neutron scintillator, neutral

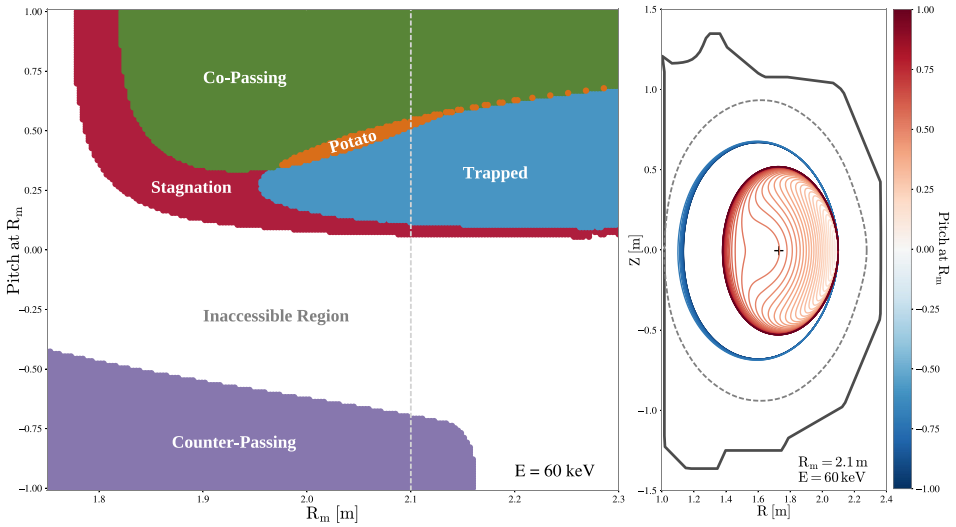

FIG. 2. Left: topological map of different orbit types[15] with fixed energy for the DIII-D plasma described in Sec. III A. Right: orbits corresponding to the dashed line in the topological map. The plus indicates the magnetic axis and the dashed line is the last-closed flux surface.

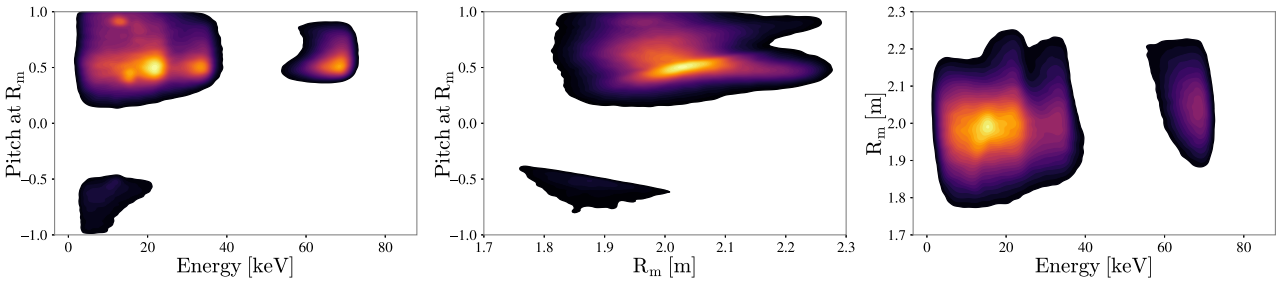

FIG. 3. Projections of the orbit-space fast-ion distribution for shot #159243 at 790 ms. Each projection is the full 3D distribution integrated over one of the variables, e.g., $F_z(x,y) = \int F(x,y,z)\,dz$. Each projection is normalized to unity.

particle analyzer (NPA), and fast-ion D-α (FIDA). The orbit weight functions are calculated on a $100 \times 100 \times 100$ element (E, p_m, R_m) grid.

A. Apparatus

The selected plasma is DIII-D shot #159243 at 790 ms. This discharge, which is discussed in detail in Ref. 16, is a reversed-shear plasma with a toroidal field of 2.0 T and plasma current of 0.8 MA. The fast-ion population is created by deuterium neutral beams of energy 70–81 keV that are injected in both the co-current and counter-current directions. Although the discharge has extensive Alfvén eigenmode activity, only the "classical" distribution function calculated by NUBEAM[17] in the absence of wave-induced transport is considered here. Projections of the orbit-space fast-ion distribution function for the shot are shown in Fig. 3.

The neutron scintillator measures the volume-averaged neutron rate. In its present configuration, the solid-state NPA diagnostic is operated in the current mode.[18] The NPA and FIDA diagnostics considered here both view the 210RT neutral beam (Fig. 4). The fast-ion diagnostic simulation code, FIDASIM,[21] has the ability to calculate the expected signal for an arbitrary fast-ion distribution for the Neutron, NPA, and FIDA diagnostics. Since an orbit weight function is just the expected signal produced by a fast ion on an orbit, FIDASIM can be used to evaluate the integral in Eq. (11) by creating a fast-ion distribution input file that consists of fast ions that are uniformly distributed along a single orbit.

B. Neutron scintillator orbit weight function

A neutron scintillator detects neutrons that are produced via the following fusion reaction:

$$D + D \rightarrow He^3 + n. \tag{12}$$

The total cross section for this reaction is given by

$$\sigma_T(E) = \frac{S(E)}{E \exp\left(B_G/\sqrt{E}\right)}, \tag{13}$$

where E is the energy in the center-of-mass frame in keV, B_G is the Gamov constant, and $S(E)$ is a Padé expansion of the astrophysical S-function.[22]

Here we consider only beam-plasma reactions, since they often predominate. The beam-plasma neutron reactivity of a fast ion interacting with a thermal background plasma is given by

$$\langle \sigma v \rangle (\mathbf{v}_f) = \int \sigma_T \left(\frac{\mu}{2} ||\mathbf{v}_f - \mathbf{v}_t||^2 \right) ||\mathbf{v}_f - \mathbf{v}_t|| f(\mathbf{v}_t)\, d\mathbf{v}_t, \tag{14}$$

where μ is the reduced mass of the fast and thermal ion species, $\mathbf{v}_f$ is the fast-ion velocity, $\mathbf{v}_t$ is the thermal-ion velocity, and f is a shifted Maxwellian velocity distribution.[23] The

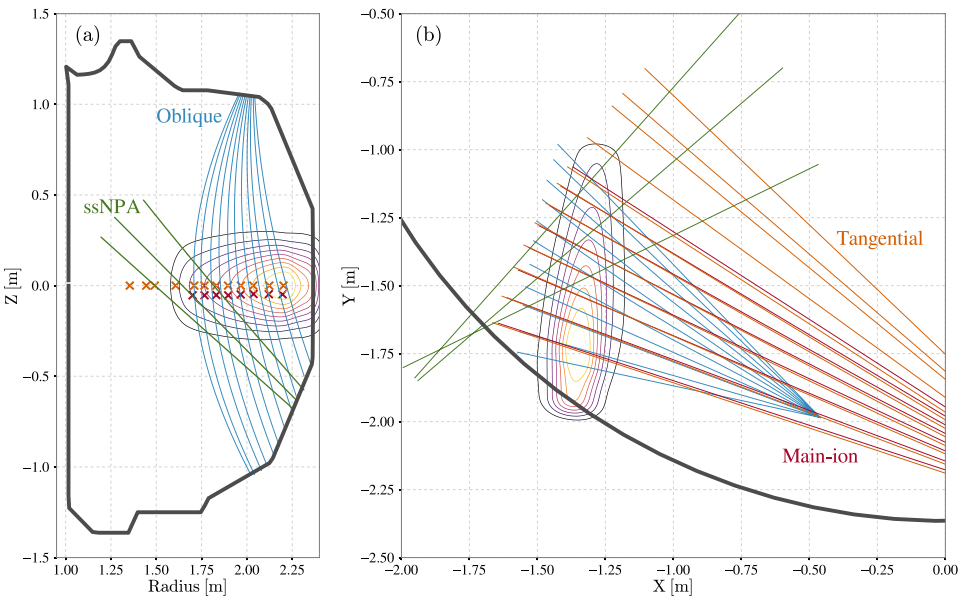

FIG. 4. Poloidal (a) and plan (b) view of the 210RT neutral beam density (contours) and fast-ion diagnostics (colored lines). The Oblique FIDA system,[19] shown in blue, consists of a maximum of 11 viewing chords looking down at the 210RT beam at an oblique angle of ∼45° with respect to the midplane. The Main-ion and Tangential spectroscopic systems,[20] shown in red and orange respectively, provide a combined 20 midplane views of the neutral beam. The solid state NPA system (ssNPA),[18] shown in green, consists of three channels viewing the core region of the plasma from below the midplane.

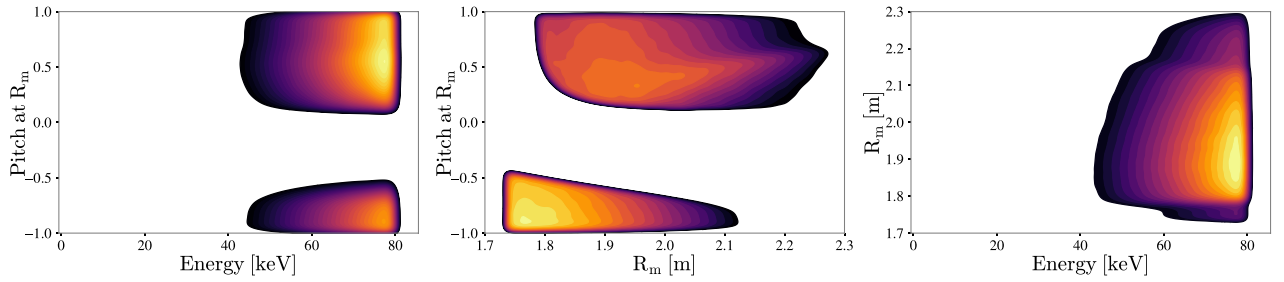

FIG. 5. Normalized projections of the 3D neutron orbit weight function.

expected signal produced by a fast ion with phase-space coordinates $\mathbf{x}$ is given by

$$S_{neut}(\mathbf{x}) = \epsilon\, d_D(\mathbf{x})\, \langle \sigma v \rangle(\mathbf{x}), \tag{15}$$

where ϵ is the detector efficiency and d_D is the thermal deuterium density. Substituting this equation into Eq. (11) yields the neutron orbit weight function (Fig. 5).

In isolation, the neutron orbit weight function gives insight into the underlying physics of the diagnostic. For example, the strong energy dependence of the orbit weight function indicates that the effect of the neutron cross section is considerable. This type of analysis can also be done using velocity-space weight functions; however, with orbit weights, the sensitivity of the diagnostic to individual orbit types can also be analyzed (Table I). Table I shows the signal produced by each orbit type, indicating that co-passing orbits produce the most signal. Somewhat surprisingly, the neutron diagnostic is quite sensitive to potato orbits despite the small volume of phase space that they occupy. This is caused by the tendency of potato orbits to spend a large fraction of their orbit in the high density core region. The total beam-plasma neutrons produced, as calculated by Eq. (8), is in agreement with the predictions of TRANSP/NUBEAM and FIDASIM (Fig. 6).

C. Neutral particle analyzer (NPA) orbit weight function

Consider a beam of fast ions traveling through a cloud of neutral particles. The fast ions can undergo the following charge exchange reaction:

TABLE I. Dependence of neutron signal on orbit topology for DIII-D discharge #159243 at 790 ms. column1: Type[15] of orbit. column 2: Average neutron signal produced by a fast ion of the given type. column3: Fraction of the fast-ion phase space occupied by the orbit type. column 4: Total neutron signal produced by each orbit type. The table indicates that the neutron diagnostic is most sensitive to potato orbits. Additionally, it shows that counter-passing orbits produce more signals on average than co-passing orbits due to counter-passing orbits traveling against the bulk plasma rotation, causing a higher relative energy.

Orbit type	Average weight (s^{-1})	Phase-space fraction	Signal produced (s^{-1})
Potato	3.83×10^{-5}	7.75×10^{-3}	1.19×10^{12}
Stagnation	3.69×10^{-5}	9.61×10^{-2}	2.86×10^{11}
Trapped	2.09×10^{-5}	2.41×10^{-1}	5.65×10^{12}
Ctr-Passing	2.82×10^{-5}	2.93×10^{-1}	3.67×10^{11}
Co-Passing	2.67×10^{-5}	3.62×10^{-1}	1.57×10^{13}
Total			2.32×10^{13}

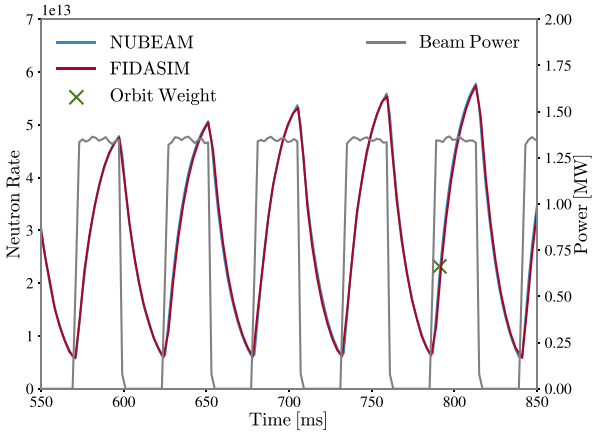

FIG. 6. Beam-plasma neutron rate and injected beam power over time for shot #159243 calculated by the NUBEAM and FIDASIM codes and the rate at 790 ms calculated using the neutron orbit weight function and Eq. (8).

$$H_f^+ + H(m) \rightarrow H_f(n) + H^+. \tag{16}$$

The energy of the newly created fast neutral, $H_f(n)$, can then be detected, forming the basis of the NPA diagnostic. Additionally, the fast neutral can be born into an excited state and relax to a lower energy state, emitting a photon. The Doppler shift of the photon contains information about the fast ion before it was neutralized. This process forms the basis of the FIDA diagnostic.

In the case of active NPA and FIDA spectroscopy, the source of donor neutrals is provided via the neutral beam injection. Neutral beam injection creates three distinct neutral populations due to acceleration of molecular hydrogen. During the neutralization phase of the neutral beam injection, the molecular forms are eliminated and the gained energy is split evenly among the atoms. The energy of each population is given by $E_i = E_1/i$ where i is the number of hydrogen atoms in each molecule. The velocity distribution of each species is tightly focused and can be approximated by a Dirac delta function. A fourth population of neutrals forms when injected neutrals charge exchange with thermal ions creating a thermal "halo" with a shifted Maxwellian velocity distribution.

The rate in which a fast ion, interacting with the k different neutral populations, produces a fast-neutral, H_f, in the nth energy level, i.e., neutral population flux, is given by

$$\mathbf{f} = \sum_k \left[\int \mathbf{X}(\mathbf{v}_f - \mathbf{v}) \cdot \mathbf{d}_k \, ||\mathbf{v}_f - \mathbf{v}|| f_k(\mathbf{v})\, d\mathbf{v} \right], \tag{17}$$

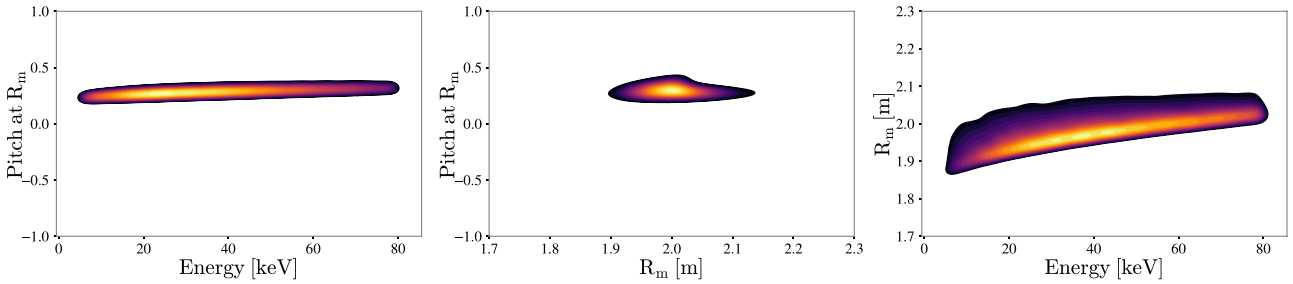

FIG. 7. Normalized projections of the ssNPA (Fig. 4) orbit weight function at R = 1.64 m for shot #159243 @ 790 ms.

where $\mathbf{X}$ [cm^2] is a $n \times m$ matrix of the charge exchange cross sections, $\mathbf{d}_k$ [cm^{-3}] is the densities vector of the m energy levels of the donor neutral, and f_k is the velocity distribution of the k^{th} neutral population.

The neutral population flux, $\mathbf{f}$, evolves as it travels through the background plasma due to collisions with the different plasma species. The effects of the different collisional processes on the population flux can be modeled by the following matrix differential equation:

$$\frac{d\mathbf{f}}{dt} = \mathbf{C} \cdot \mathbf{f}, \tag{18}$$

where $\mathbf{C}$ is a matrix of the rate coefficients for the various collisional and atomic transitions. The full derivation of Eq. (18) is given in the Appendix.

The solution of Eq. (18) takes the form of a matrix exponential

$$\mathbf{f}(t) = e^{\mathbf{C}t} \cdot \mathbf{f}(0) = \mathbf{S} \cdot e^{\mathbf{\Lambda} t} \cdot \mathbf{S}^{-1} \cdot \mathbf{f}(0), \tag{19}$$

where $\mathbf{f}(t)$ is a vector of the neutral population flux [1/s] at time t, $\mathbf{S}$ is the matrix of the eigenvectors of $\mathbf{C}$, and $\mathbf{\Lambda}$ is a diagonal matrix containing the eigenvalues of $\mathbf{C}$. Equation (18) depends on the local plasma parameters and is solved iteratively along the trajectory of the neutral.

Should the trajectory of the neutral particle enter the NPA detector, the expected NPA signal is then given by

$$S_{NPA}(\mathbf{x}) = \epsilon(E) \sum_n \mathbf{f}(t_{det}), \tag{20}$$

where t_{det} is the travel time to the detector and $\epsilon(E)$ is an energy-dependent detector efficiency. Substituting this equation into Eq. (11) gives the orbit weight function for the NPA diagnostic (Fig. 7).

Figure 7 shows that the NPA diagnostic is localized in space (R_m) and in pitch (p_m) but, because the detector is operated in current mode, the weight function is sensitive to a large swath of energies. The localization in space and pitch is caused by the narrow collimation of the ssNPA diagnostic. Figure 8 shows that the energy resolved NPA flux calculated using the NPA orbit weights agrees with FIDASIM.

D. Fast-ion D-α spectroscopy (FIDA) orbit weight function

The number of neutrals after a time t, $\mathbf{n}(t)$, is found by integrating Eq. (19)

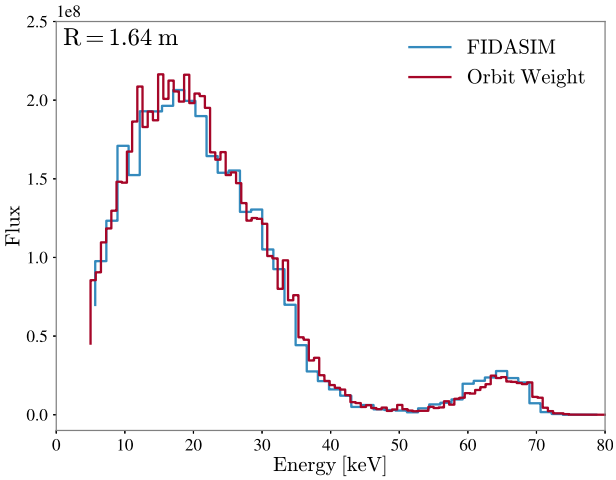

FIG. 8. Comparison of the energy resolved NPA flux for shot #159243 @ 790 ms calculated by FIDASIM and by the NPA orbit weight functions and Eq. (8).

$$\mathbf{n}(t) = \mathbf{S} \cdot (\mathbf{\Lambda}^{-1} \cdot e^{\mathbf{\Lambda} t} - \mathbf{\Lambda}^{-1}) \cdot \mathbf{S}^{-1} \cdot \mathbf{f}(0). \tag{21}$$

If t represents the time spent inside a measurement volume, V, the Balmer-α photon flux is given by

$$\Phi_\gamma = n_3(t)\, A_{3\to 2}, \tag{22}$$

where $A_{3\to 2}$ is the spontaneous emission rate for the D-α transition. The photon radiance can then be calculated by integrating the photon flux density per steradian over the line of sight,

$$L_\gamma = \frac{1}{4\pi V} \int_{LOS} \Phi_\gamma \, dl. \tag{23}$$

In the presence of a magnetic field, the motion of an ion will induce an electric field, breaking the spherical symmetry of the atom. This allows for the existence of multiple stable states that have the same principle quantum number n. This effect is called Motional Stark splitting. For hydrogenic atoms, the differences in the energy between the states are linear in electric field strength and are given by

$$\Delta\mathcal{E}(n) = \frac{3\, n\, k\, a_0}{2} E \;\forall k : |k| < n \quad [\text{eV}], \tag{24}$$

where a_0 is the Bohr radius and E is the magnitude of the induced electric field.[24] As seen from the above equation, the

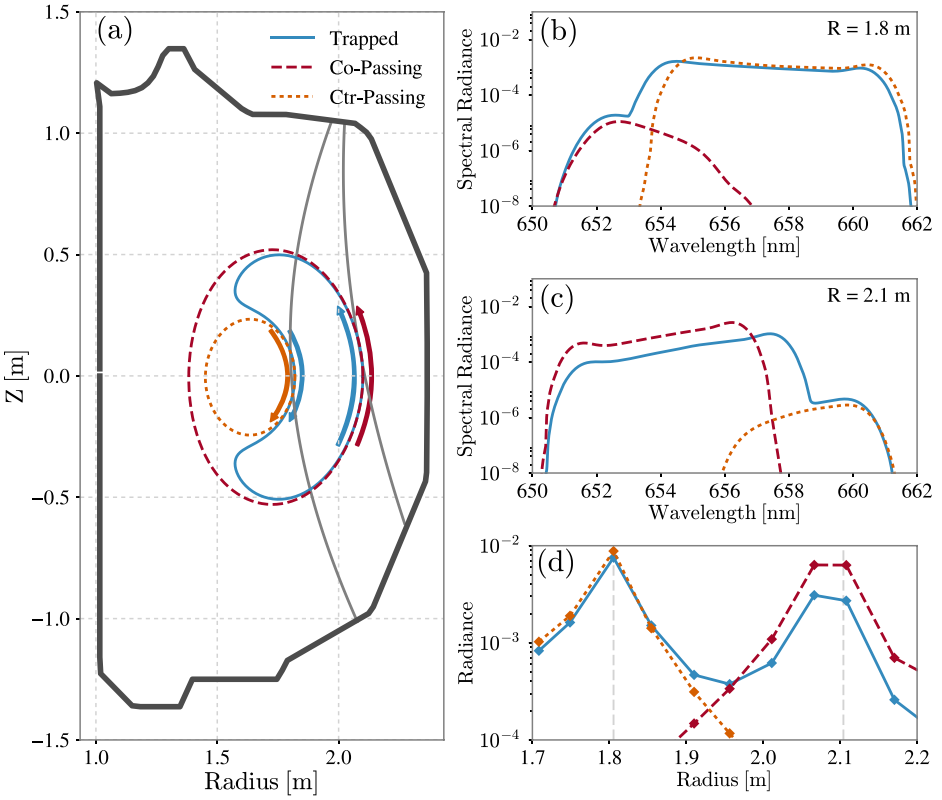

FIG. 9. FIDA orbit weights/spectra produced by three different orbits: trapped [$\mathbf{J} = (50\,\text{keV}, 0.5, 2.1\,\text{m})$], co-passing [$\mathbf{J} = (50\,\text{keV}, 0.7, 2.1\,\text{m})$], and counter passing [$\mathbf{J} = (50\,\text{keV}, -0.5, 1.82\,\text{m})$]. Arrows indicate direction of the fast-ion poloidal velocity. (a) Polodial projection of the orbits and oblique FIDA chords. (b) FIDA spectra produced by the orbits at $R = 1.8\,\text{m}$. (c) FIDA spectra produced by the orbits at $R = 2.1\,\text{m}$. (d) Radial profile of FIDA spectra integrated from 647 to 667 nm.

number of states for each principle quantum number is given by $2n - 1$. The transition from $n = 3 \rightarrow 2$ creates 15 distinct spectral lines whose wavelength shifts are given by

$$\Delta\lambda_{lk} = \frac{3\lambda_0^2\, a_0(3l - 2k)}{2hc} E \quad \forall C(l,k) : (|l| < 3) \wedge (|k| < 2), \tag{25}$$

where λ_0 is the unshifted wavelength (656.1 nm).[25] After also taking into account the Doppler shift due to the line of sight geometry, the wavelength for each Stark line is

$$\lambda_{lk} = \lambda_0(1 + \Delta\lambda_{lk}/\lambda_0 + (\hat{\omega} \cdot \mathbf{v}_f)/c), \tag{26}$$

where $\hat{\boldsymbol{\omega}}$ is a unit vector pointing toward the collection optics.

The photon radiance given in Eq. (23) is distributed among the Stark lines. The relative radiance of each Stark line is given by

$$I_{lk} = A_{lk}\,(1 \pm (\hat{\boldsymbol{\omega}} \cdot \mathbf{E})^2), \tag{27}$$

where the expression in the parentheses is the angular distribution of the emission for the $\sigma(+)$ and $\pi(-)$ Stark lines and A_{lk} is the transition probability.[24]

The expected signal produced by a single fast ion is given by

$$S_{FIDA}(\lambda; \mathbf{x}) = \sum_{lk} \frac{L_\gamma\, I_{lk}}{\sum_{lk} I_{lk}}\, \delta(\lambda - \lambda_{lk}). \tag{28}$$

Inserting this equation into Eq. (11) completes the calculation.

The FIDA orbit weight functions depend on wavelength [Figs. 9(b) and 9(c)]. Figure 9(d) shows how different spatial locations are weighted by the orbits. For instance, if we consider the orbit weight function for a red shifted wavelength (Fig. 10), we can see that the chord (oblique@1.9 m) sees the signal from counter-passing particles localized at $R_m = 1.91\,\text{m}$ and also trapped particles from as far out as $R_m = 2.18\,\text{m}$. The spectra calculated using orbit weight functions closely matches the spectra produced by FIDASIM (Fig. 11).

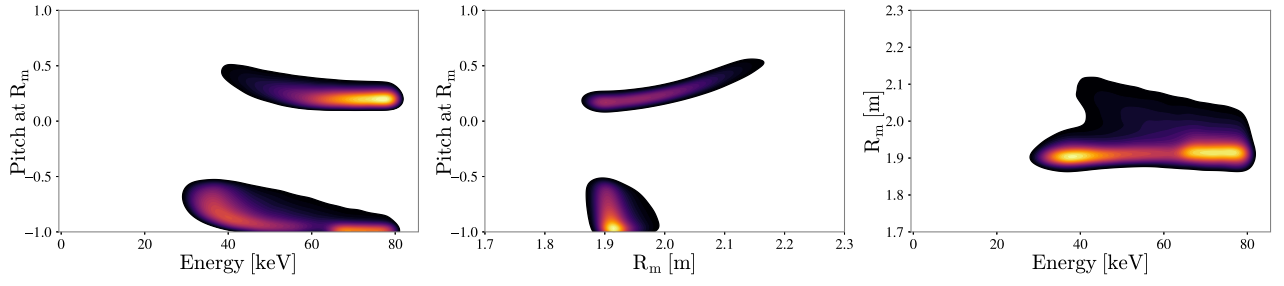

FIG. 10. Projections of the red shifted ($\lambda = 660 \pm 0.2\,\text{nm}$) FIDA orbit weight function for an oblique viewing chord with midplane intersection at $R = 1.9\,\text{m}$.

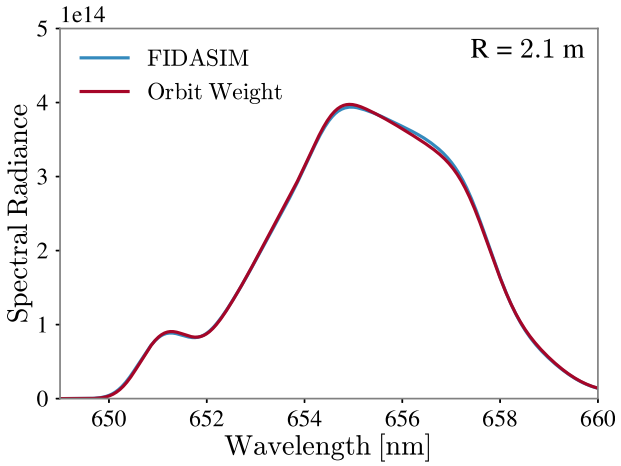

FIG. 11. FIDA Spectra for shot #159243 @ 790 ms calculated by FIDASIM and by the FIDA orbit weight functions and Eq. (8) for an oblique (Fig. 4) viewing chord at $R = 2.1$ m.

Orbit weight functions are more accurate than velocity-space weight functions. Figure 12 shows spectra calculated using spatially-averaged velocity-space weight functions. Near the magnetic axis [Fig. 12(a)], the calculated spectrum agrees well with FIDASIM, indicating that the velocity-space method is accurate. However, off-axis [Fig. 12(b)], the spectrum calculated with spatially averaged velocity-space weight functions deviates from FIDASIM. Comparisons with simulations that use a uniform fast-ion distribution are not discrepant, showing that spatial variations are responsible for the deviation. Generally, as in Fig. 12, velocity-space weight functions work better near the magnetic axis, where spatial gradients are relatively smaller, than in the periphery, where variations in the fast-ion density and other quantities tend to be large.

IV. CONCLUSION AND FUTURE WORK

Diagnostic signals calculated using 2D velocity-space weight functions can be inaccurate when the fast-ion distribution changes rapidly within the measurement volume. Using a 6D weight function, we can exactly model the diagnostic signal for an arbitrary fast-ion distribution. Additionally, changing to an action-angle coordinate system allows for the 6D weight function to be reduced to a 3D orbit-space weight function without losing the ability to correctly model the diagnostic signal produced by an arbitrary fast-ion distribution. In this framework, the process of deriving weight functions reduces to calculating the signal produced by a single fast ion at an arbitrary 6D phase-space coordinate and then averaging over an orbit's trajectory. Since the equilibrium fields that determine the orbits are often known quite accurately, this procedure utilizes additional information without introducing the appreciable error.

In future work, orbit weight functions will define a common interface for fast-ion diagnostics. This will allow diagnostic signals to be combined to infer the full fast-ion distribution function from experimental measurements, i.e., orbit tomography. This will greatly improve our ability to diagnose fast-ion behavior during a discharge.

ACKNOWLEDGMENTS

Useful discussions with M. Salewski are gratefully acknowledged. This work was supported by the U.S. Department of Energy under DE-AC02-09CH11466 and DE-FC02-04ER54698.

APPENDIX: COLLISIONAL RADIATIVE MODEL

The collisions that the fast-neutral experiences as it travels through a plasma changes the distribution of its energy level population. The collisional radiative model assumes that the populations of excited states with the same principal quantum number n are distributed according to a Boltzmann distribution. This allows us to only consider transitions between different energy levels. However, this assumption has been shown[26] to break down when the electron density is less than $10^{14}\,\mathrm{cm}^{-3}$. In this regime, the following collisional radiative model can overestimate the D-α emission by about 20%–25%. This remains a source of error in our model.

The types of collisions that the model considers are as follows:

- Spontaneous transitions: $A_{m\to n}/A_{n\to m}$.
- Electron/ion/impurity-impact excitation/de-excitation: $q^{e|i|Z}_{m\to n}/q^{e|i|Z}_{n\to m}$.
- Electron/ion/impurity-impact ionization: $I^{e|i|Z}_{n}$.
- Charge exchange with ions/impurities: $X^{i|Z}_{n}$.

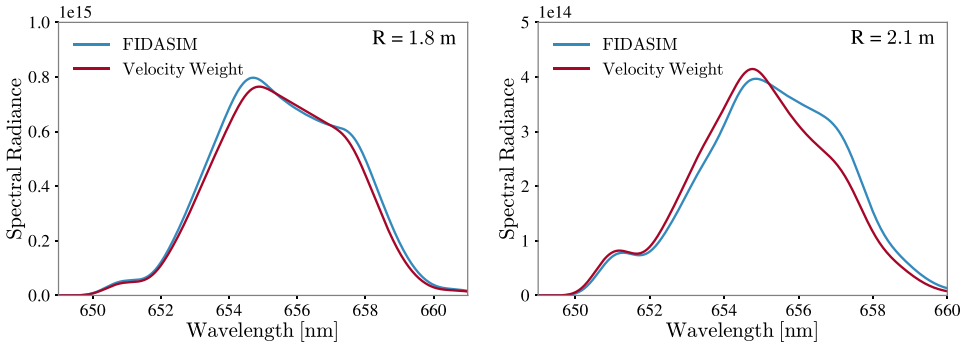

FIG. 12. FIDA spectra calculated using spatially-averaged velocity-space weight functions [Eq. (1)] for the oblique viewing chords at (a) $R = 1.8$ and (b) $R = 2.1$ m. The spectra calculated by FIDASIM are also shown. Disagreement between FIDASIM and Eq. (1) is because the latter uses a spatially averaged fast-ion distribution to calculate the spectra. Differences between the spatially averaged distribution and the full distribution used by FIDASIM cause the two methods to disagree to varying degrees.

With the exception of the spontaneous transitions which have units of s^{-1}, the above rate coefficients have units of cm^3/s and are calculated by averaging the respective collisional cross sections with a Maxwellian of the relevant species.

The quasi-static equilibrium population flux of the nth energy level of a neutral atom, f_n, can be described by the following time dependent differential equation:

$$\begin{aligned}\frac{df_n}{dt} = &-\left(\sum_{k=i,Z} f_n d_k X_n^k + \sum_{k=e,i,Z} f_n d_k I_n^k\right)\\ &+\sum_{m>n}\left(f_m A_{m\to n} + \sum_{k=e,i,Z}\left(f_m d_k q_{m\to n}^k - f_n d_k q_{n\to m}^k\right)\right)\\ &+\sum_{n>m}\left(-f_n A_{n\to m} + \sum_{k=e,i,Z}\left(f_m d_k q_{m\to n}^k - f_n d_k q_{n\to m}^k\right)\right),\end{aligned}$$

where the d_k are the respective target densities.

Rearranging terms and letting $q_{n\to m}^k$ represent excitation/de-excitation depending on the order of the indices yields the following equation:

$$\frac{df_n}{dt} = C_{nn} f_n + \sum_{m\neq n} C_{nm} f_m, \tag{A1}$$

where

$$C_{nn} = -\left[\sum_{k=i,Z} d_k X_n^k + \sum_{k=e,i,Z} d_k I_n^k + \sum_{m\neq n}\left(A_{n\to m} + \sum_{k=e,i,Z} d_k q_{n\to m}^k\right)\right], \tag{A2}$$

and

$$C_{nm} = A_{m\to n} + \sum_{k=e,i,Z} d_k q_{m\to n}^k. \tag{A3}$$

The system of differential equations can be compactly represented as a matrix multiplication

$$\frac{d\mathbf{f}}{dt} = \mathbf{C}\cdot\mathbf{f}. \tag{A4}$$

[1]W. W. Heidbrink, Y. Luo, K. H. Burrell, R. W. Harvey, R. I. Pinsker, and E. Ruskov, "Measurements of fast-ion acceleration at cyclotron harmonics using balmer-alpha spectroscopy," Plasma Phys. Controlled Fusion **49**(9), 1457 (2007).

[2]M. Salewski, S. K. Nielsen, H. Bindslev, V. Furtula, N. N. Gorelenkov, S. B. Korsholm, F. Leipold, F. Meo, P. K. Michelsen, D. Moseev *et al.*, "On velocity space interrogation regions of fast-ion collective thomson scattering at ITER," Nucl. Fusion **51**(8), 083014 (2011).

[3]M. Salewski, B. Geiger, D. Moseev, W. W. Heidbrink, A. S. Jacobsen, S. B. Korsholm, F. Leipold, J. Madsen, S. K. Nielsen, J. Rasmussen *et al.*, "On velocity-space sensitivity of fast-ion d-alpha spectroscopy," Plasma Phys. Controlled Fusion **56**(10), 105005 (2014).

[4]A. S. Jacobsen, M. Salewski, J. Eriksson, G. Ericsson, S. B. Korsholm, F. Leipold, S. K. Nielsen, J. Rasmussen, M. Stejner, and J. E. T. EFDA others, "Velocity-space sensitivity of neutron spectrometry measurements," Nucl. Fusion **55**(5), 053013 (2015).

[5]M. Salewski, M. Nocente, G. Gorini, A. S. Jacobsen, V. G. Kiptily, S. B. Korsholm, F. Leipold, J. Madsen, D. Moseev, S. K. Nielsen *et al.*, "Velocity-space observation regions of high-resolution two-step reaction gamma-ray spectroscopy," Nucl. Fusion **55**(9), 093029 (2015).

[6]M. Salewski, M. Nocente, G. Gorini, A. S. Jacobsen, V. G. Kiptily, S. B. Korsholm, F. Leipold, J. Madsen, D. Moseev, S. K. Nielsen *et al.*, "Fast-ion energy resolution by one-step reaction gamma-ray spectrometry," Nucl. Fusion **56**(4), 046009 (2016).

[7]M. Salewski, B. Geiger, S. K. Nielsen, H. Bindslev, M. García-Muñoz, W. W. Heidbrink, S. B. Korsholm, F. Leipold, F. Meo, P. K. Michelsen *et al.*, "Tomography of fast-ion velocity-space distributions from synthetic cts and fida measurements," Nucl. Fusion **52**(10), 103008 (2012).

[8]M. Salewski, B. Geiger, S. K. Nielsen, H. Bindslev, M. García-Muñoz, W. W. Heidbrink, S. B. Korsholm, F. Leipold, J. Madsen, F. Meo *et al.*, "Combination of fast-ion diagnostics in velocity-space tomographies," Nucl. Fusion **53**(6), 063019 (2013).

[9]M. Salewski, B. Geiger, A. S. Jacobsen, M. García-Muñoz, W. W. Heidbrink, S. B. Korsholm, F. Leipold, J. Madsen, D. Moseev, S. K. Nielsen *et al.*, "Measurement of a 2d fast-ion velocity distribution function by tomographic inversion of fast-ion d-alpha spectra," Nucl. Fusion **54**(2), 023005 (2014).

[10]A. S. Jacobsen, L. Stagner, M. Salewski, B. Geiger, W. W. Heidbrink, S. B. Korsholm, F. Leipold, S. K. Nielsen, J. Rasmussen, M. Stejner *et al.*, "Inversion methods for fast-ion velocity-space tomography in fusion plasmas," Plasma Phys. Controlled Fusion **58**(4), 045016 (2016).

[11]F. Jaulmes, B. Geiger, T. Odstrčil, M. Weiland, M. Salewski, A. S. Jacobsen, J. Rasmussen, M. Stejner, S. K. Nielsen, E. Westerhof *et al.*, "Numerical and experimental study of the redistribution of energetic and impurity ions by sawteeth in ASDEX upgrade," Nucl. Fusion **56**(11), 112012 (2016).

[12]M. Weiland, B. Geiger, A. S. Jacobsen, M. Reich, M. Salewski, and T. Odstrčil, "Enhancement of the fida diagnostic at ASDEX upgrade for velocity space tomography," Plasma Phys. Controlled Fusion **58**, 025012 (2016).

[13]J. A. Rome and Y. K. M. Peng, "The topology of tokamak orbits," Nucl. Fusion **19**(9), 1193 (1979).

[14]Y. V. Petrov and R. W. Harvey, "A fully-neoclassical finite-orbit-width version of the cql3d fokker–planck code," Plasma Phys. Controlled Fusion **58**(11), 115001 (2016).

[15]R. B. White, *The Theory of Toroidally Confined Plasmas*, 3rd ed. (Imperial College Press, London, 2014), Sec. 3.3.

[16]W. W. Heidbrink, C. S. Collins, M. Podestà, G. J. Kramer, D. C. Pace, C. C. Petty, L. Stagner, M. A. Van Zeeland, R. B. White, and Y. B. Zhu, "Fast-ion transport by Alfvén eigenmodes above a critical gradient threshold," Phys. Plasmas **24**(5), 056109 (2017).

[17]A. Pankin, D. McCune, R. Andre, G. Bateman, and A. Kritz, "The tokamak monte carlo fast ion module nubeam in the national transport code collaboration library," Comput. Phys. Commun. **159**, 157 (2004).

[18]Y. B. Zhu, A. Bortolon, W. W. Heidbrink, S. L. Celle, and A. L. Roquemore, "Compact solid-state neutral particle analyzer in current mode," Rev. Sci. Instrum. **83**(10), 10D304 (2012).

[19]C. M. Muscatello, W. W. Heidbrink, D. Taussig, and K. H. Burrell, "Extended fast-ion d-alpha diagnostic on diii-d," Rev. Sci. Instrum. **81**(10), 10D316 (2010).

[20]B. A. Grierson, K. H. Burrell, C. Chrystal, R. J. Groebner, D. H. Kaplan, W. W. Heidbrink, J. M. M. Burgos, N. A. Pablant, W. M. Solomon, and M. A. Van Zeeland, "Active spectroscopic measurements of the bulk deuterium properties in the diii-d tokamak," Rev. Sci. Instrum. **83**(10), 10D529 (2012).

[21]L Stagner and B Geiger, http://d3denergetic.github.io/FIDASIM/ for FIDASIM: A Neutral Beam and Fast-ion Diagnostic Modeling Suite.

[22]H.-S. Bosch and G. M. Hale, "Improved formulas for fusion cross-sections and thermal reactivities," Nucl. Fusion **32**(4), 611 (1992).

[23]The bulk plasma rotation shifts the Maxwellian distribution.

[24]H. A. Bethe and E. E. Salpeter, *Quantum Mechanics of One-and Two-Electron Atoms* (Springer Science & Business Media, 2012).

[25]This equation is derived via the Taylor expansion of the Rydberg equation.

[26]O. Marchuk, Y. Ralchenko, and D. R. Schultz, "Non-statistical population distributions for hydrogen beams in fusion plasmas," Plasma Phys. Controlled Fusion **54**(9), 095010 (2012).